Journal of Power Sources 669 (2026) 239403

Contents lists available at ScienceDirect

Journal of Power Sources

journal homepage: www.elsevier.com/locate/jpowsour

Vanadium telluride VTe_2: a novel cathode for rechargeable aluminum batteries and its performance optimization

Rafael Córdoba [a,b,*], Ruocun (John) Wang [c,d], Vanessa Trouillet [a], Sonia Dsoke [a,e,f,g]

[a] Institute for Applied Materials (IAM), Karlsruhe Institute of Technology (KIT), Hermann-von-Helmholtz-Platz 1, D-76344, Eggenstein-Leopoldshafen, Germany
[b] Departamento de Química y Bioquímica, Facultad de Farmacia, Universidad San Pablo-CEU, Madrid, 28668, Spain
[c] Department of Materials Science and Engineering and A. J. Drexel Nanomaterials Institute, Drexel University, Philadelphia, PA, 19104, United States
[d] Department of Materials Science and Engineering, University of North Texas, Denton, TX, 76207, United States
[e] Fraunhofer Institute for Solar Energy Systems, Dep. Electrical Energy Storage, Heidenhofstr. 2, Freiburg, 79110, Germany
[f] FMF—Freiburg Materials Research Center, University of Freiburg, Stefan-Meier Str. 21, Freiburg, 79104, Germany
[g] Institute for Sustainable Systems Engineering (INATECH), University of Freiburg, Emmy-Noether-Straße 2, Freiburg, 79110, Germany

HIGHLIGHTS

- VTe_2 is introduced as a new cathode material for rechargeable aluminum batteries.
- Electrochemical activity comes from V^{5+}/V^{4+} and Te^{4+}/Te^{2-} redox pairs.
- Charge storage mechanism is based on interaction with $AlCl_4^-$ anions.
- $Ti_3C_2T_x$ and CMK-3 modified separators mitigate shuttle effect and extend cycling.
- VTe_2 performance improves from 10 mAh g^{-1} (cycle 75) to 63 mAh g^{-1} (cycle 300).

ARTICLE INFO

Keywords:
Electrochemistry
Aluminum batteries
Cathodes
Transition metal chalcogenides
Vanadium
Tellurides
MXene

ABSTRACT

Vanadium telluride VTe_2 has been successfully synthesized via hydrothermal reaction and characterized for the first time as a cathode for rechargeable aluminum batteries. The electrochemical activity of VTe_2 originates from the redox pairs Te^{4+}/Te^{2-} and V^{5+}/V^{4+}. VTe_2 delivers a first discharge capacity of 275 mAh g^{-1} at 100 mA g^{-1} vs. an Al anode. The charge transport within VTe_2 is based on interaction with $AlCl_4^-$ anions, while the charge storage mechanism is dominated by surface-controlled processes at low voltages and by diffusion-controlled processes at high voltages. However, VTe_2 suffers a rapid, drastic capacity loss and a short cycle life (<100 cycles) due to the corrosive chloroaluminate electrolyte, which dissolves the cathode active material upon charging and causes the shuttle effect. $Ti_3C_2T_x$ MXene (forming a composite with VTe_2) and CMK-3 mesoporous carbon (embedded onto the separators) are used as strategies to avoid the shuttle effect of soluble species towards the anode. This enables the reversibility of the redox reaction, allowing VTe_2 to develop a sustained electrochemical activity. $VTe_2/Ti_3C_2T_x$ composite with CMK-3 modified separators shows improved electrochemical performance over as-prepared VTe_2: 63 mAh g^{-1} after 300 cycles vs. 10 mAh g^{-1} after 75 cycles at 100 mA g^{-1}.

1. Introduction

In the last decades, energy storage has become crucial, as society has been trying to carry out the transition from fossil fuels to more environmentally friendly technologies, such as rechargeable batteries. During this time, Li-ion batteries (LIBs) have been the most prominent energy storage technology due to their outstanding electrochemical performance [1,2]. However, due to LIBs success and the exponential demand for batteries that comes with global electrification, world lithium resources are draining, causing the price of LIBs to increase [3]. To alleviate this situation, researchers explore alternative energy storage systems, aiming to develop the so-called post-lithium batteries. During the last decades, several post-lithium battery chemistries based on different metals have been widely explored, *e.g.*, sodium [4,5],

* Corresponding author.
E-mail addresses: rafael.cordobarojano@ceu.es, rafael.rojano@kit.edu (R. Córdoba).

https://doi.org/10.1016/j.jpowsour.2026.239403
Received 23 June 2025; Received in revised form 15 January 2026; Accepted 20 January 2026
Available online 2 February 2026
0378-7753/© 2026 The Authors. Published by Elsevier B.V. This is an open access article under the CC BY license (http://creativecommons.org/licenses/by/4.0/).

magnesium [6], potassium [7,8], calcium [9], zinc [10,11] or aluminum [12–15].

Among such post-lithium batteries, rechargeable aluminum batteries (RABs) are an interesting alternative to LIBs for several reasons: sustainability, as aluminum is the most abundant metal element in the earth's crust and has well-established recyclability; high theoretical volumetric capacity, almost four times higher than lithium; and safety, because of the excellent air stability of aluminum metal [16–18]. However, RABs are in an early stage of development (just in 2015, the first RAB prototype with proper reversibility was developed at a lab scale [19]), so scientific efforts have been focused on overcoming technical issues during this phase. For instance, designing a suitable electrolyte for RABs has been a challenge [20] until it was discovered that the ionic-liquid (IL) mixture of $AlCl_3$ and 1-ethyl-3-methylimidazolium chloride (EMImCl) enables reversible plating and stripping of aluminum [21]. Nevertheless, its highly acidic, corrosive nature makes it difficult not only to find proper cathodes, but also other components of the cell, such as the binder and the current collector, which can be dissolved and corroded [22]. It has been reported that the most common materials employed as current collectors in other battery systems (aluminum, copper, stainless steel and more) undergo electrochemical reactions with the electrolyte [23]. Molybdenum foil is widely used as a current collector for RABs, but it also reacts with the electrolyte at high voltage values, above 1.8 V [24], especially after several charge-discharge cycles. Something similar happens with the binder: the acidic electrolyte can dissolve and react with the most common binders, such as polyvinylidene fluoride (PVDF) [25] and carboxymethyl cellulose (CMC) [26]. The cathode material must be subjected to thorough scrutiny because the other cell components easily interact with the electrolyte, leading to electrochemical activity coming from them and not from the active cathodic material [21,27]. Another drawback caused by the corrosivity of the electrolyte is the hindered application of certain advanced, *operando* analysis techniques to RABs, which can be addressed by designing and developing special types of cells for *in situ* measurements. Concerning more technical issues that RABs may afront because of the electrolyte, the cost of the battery can be mitigated by the cost-effective aluminum metal used as anode [28], and regarding large-scaling, it can be helped by the existing research on other RABs electrolytes for industrial-scale aluminum plating [29].

Since graphite was employed in the first lab-scale prototype by Lin et al. [19], it has been considered the most used cathode for RABs due to its high operating voltage (about 2.3 V vs. Al anode) and long lifetime [30]. However, graphite as a RAB cathode shows some drawbacks, such as its low specific capacity and sustainability issues [31]. The charge storage mechanism of graphite, like many other RAB cathode materials, is based on an $AlCl_4^-$ anion insertion mechanism, known as the dual-ion mechanism because both $AlCl_4^-$ and $Al_2Cl_7^-$ anions are involved in the electrochemical activity at the cathode and anode, respectively. On the one hand, $AlCl_4^-$ anion species are incorporated into the cathode during charging, and on the other hand, the electroplating of aluminum, originating from $Al_2Cl_7^-$ anions, takes place at the anode. In dual-ion batteries, the electrolyte acts as a) a medium for ionic contact between the cathode and the anode and b) an active component of the cell, being the source of the $AlCl_4^-$ and $Al_2Cl_7^-$ anions required for electrochemical energy storage. As a result, the charge storage mechanism of dual-ion RABs differs significantly from that of rocking chair metal-ion batteries, where the electrolyte acts solely as a carrier of the ions [32]. A fair number of different compounds have been reported to be suitable cathodes for RABs, such as carbon-based materials [15,33], transition metal oxides [34,35], polymeric compounds [36] and transition metal chalcogenides (TMCs).

TMCs are an appealing family of RAB cathodes due to their abundance, high capacity and high electronic conductivity. Some examples of TMCs with interesting electrochemical performance in terms of specific capacity and cycle life are NiTe [37], $Cu_{1.81}Te$ [23], VS_2 [38], VS_4 [39,40] and VSe_2 [41] (see Table S1). However, the voltage value vs. Al anode at which their electrochemical processes take place is rather low, barely exceeding 1 V. In addition, their electrochemical stability could be improved by avoiding the dissolution of the active material. Vanadium telluride has attracted our interest for several reasons. On the one hand, vanadium is an interesting transition metal because of its rich redox chemistry and variety of oxidation states, which explains the great number of vanadium-based cathodes in other battery systems [42,43]. On the other hand, tellurides usually exhibit a higher electronic conductivity compared to sulfides or selenides, given the higher conductivity of Te (2×10^2 S cm^{-1}) than that of S (5×10^{-16} S cm^{-1}) or Se (1×10^{-4} S cm^{-1}) [44]. In addition, tellurium has the largest ionic radius among the chalcogens, leading to larger unit cell volumes, which entails the accommodation of ions and mitigates the volume effect caused by ions (de)insertion [45]. Finally, VTe_2 has been thoroughly studied for other battery systems, such as an agent to prevent the shuttle effect of polysulfides in Li-S batteries [46] or as a cathode for Zn-ion batteries [47], albeit it is the only vanadium chalcogenide that has not yet been studied as a cathode for RABs so far.

However, TMCs present a main setback when used as cathodes for RABs: they suffer from side reactions with the Lewis acidic electrolyte, leading to the dissolution of the active material. Specifically within tellurides, $AlCl_4^-$ ions from the electrolyte are prone to interact with Te^{2-} ions to form the soluble species AlTeCl [44]. In addition, Te_n^{2+} polycationic clusters resulting from the electrochemical oxidation of Te^{2-} (similar to the well-known S_n^{2-} polysulfides from Li-S batteries), interact with $AlCl_4^-$ ions as well, forming soluble $Te_n(AlCl_4)_2$ [48,49]. Te^{4+} ions, also originating from the electrochemical redox reaction, tend to form the ionic complex $TeCl_3^+$ in the $AlCl_3$-EMImCl electrolyte [50,51], leading to the soluble $TeCl_3AlCl_4$ compound. As a result, these soluble species can undergo a shuttle effect and diffuse through the separator, causing a progressive loss of the active material from the electrode and, thus, an irreversible capacity fading. In order to alleviate the dissolution of TMCs, several approaches have been followed, such as the preparation of composites [44] or the use of modified separators [37,52]. These strategies retain the TMC on the cathode side, preventing the loss of material due to the shuttle effect towards the anode and allowing the soluble compounds, originating from the electrochemical oxidation reaction (like $TeCl_3AlCl_4$ and $Te_n(AlCl_4)_2$), to be reduced back at the cathode side.

Herein, VTe_2 synthesized through a hydrothermal method has been characterized for the first time as a cathode for RABs. Cell components were carefully selected considering their potential reactivity with the acidic electrolyte. To mitigate the shuttle effect of soluble species and retain the active material at the cathode side, a synergistic approach was employed by compositing $Ti_3C_2T_x$ MXene with VTe_2, and by modifying the separator with CMK-3 mesoporous carbon. Moreover, this work has shed light on the kinetics of the redox reactions involved in the transport of $AlCl_4^-$ ions in VTe_2 through the characterization of its charge storage mechanism. The results presented here constitute another example of the attractive electrochemical properties of tellurides (and TMCs in general) and their potential as promising cathodes for advanced electrochemical storage systems, such as RABs.

2. Experimental section

2.1. Synthesis of VTe_2

All the reactants were purchased from Sigma-Aldrich. The synthesis route followed was previously reported by Sree Raj et al. [53] In Solution A, 5 mmol of NH_4VO_3 (99 %) were dispersed in 30 mL of water using magnetic stirring and ultrasonication. In another Solution B, 85 mg of TeO_2 (99 %) were subjected to reduction with an excess of hydrazine hydrate (98 %). After 1 h of stirring, Solution B was carefully added to Solution A. Once the solution became homogeneous and transferred into a Teflon hydrothermal autoclave, the reactants were heated at 200 °C for 2 h. In order to synthesize the $VTe_2/Ti_3C_2T_x$

composite, 80 mg of $Ti_3C_2T_x$ were added to Solution A. The choice of this amount of MXene was taken on the basis of the mentioned work [53] (see Supporting Information). The balanced chemical reaction for the described synthesis (Eq. (1)) is the following:

$$4\ TeO_2 + 2\ NH_4VO_3 + 5\ N_2H_4 \cdot H_2O \rightarrow 2\ VTe_2 + 19\ H_2O + 6\ N_2 \quad \text{Eq. 1}$$

2.2. Synthesis of $Ti_3C_2T_x$

The synthesis of $Ti_3C_2T_x$ follows what was reported by Mathis et al. [54] In short, the stoichiometric Ti_3AlC_2 MAX phase was made by sintering a mixture of TiC (Alfa Aesar, 99.5 %), Ti (Alfa Aesar, 99.5 %), and Al (Alfa Aesar, 99.5 %) powders in a molar ratio of 2:1.25:2.2 at 1380 °C for 2 h under Ar gas flow. The heating and cooling rates were 3 °C min^{-1}. The sintered Ti_3AlC_2 MAX phase was milled down to powders using a TiN-coated milling bit and washed with 9 M HCl (Fisher Scientific) to remove impurities. The acid-washed powders were washed with DI water until pH 7, dried in a vacuum oven at 80 °C, and sieved through a 400-mesh (38 μm) sieve. To make $Ti_3C_2T_x$ MXenes, 1 g of the Ti_3AlC_2 MAX is mixed with 20 mL of etchant (6:3:1 vol ratios of 12 M HCl (Fisher Scientific), DI water, and 50 wt% HF [Acros Organics]) at 350 rpm at 35 °C for 24 h. The etched multi-layer $Ti_3C_2T_x$ MXene was washed with DI water until pH 6. The multi-layer $Ti_3C_2T_x$ MXene was dispersed in 50 mL 0.5 M LiCl at 400 rpm for 4 h to intercalate Li-ions. The Li-intercalated $Ti_3C_2T_x$ MXene was washed with DI water to remove excess Li-ions in the solution. After that, the Li-intercalated multi-layer $Ti_3C_2T_x$ MXene was delaminated via mechanical agitation and collected by repeated centrifugation and collection of supernatants. The supernatants contain the delaminated single-layer $Ti_3C_2T_x$ MXene and are kept in the refrigerator for storage.

2.3. Morphological and structural characterization

The morphological characterization of the synthesized compounds was carried out by scanning electron microscopy (SEM) using a Zeiss Supra 55 microscope (primary energy: 15 eV). Structural characterization was performed by means of X-ray diffraction (XRD) using a high-resolution diffractometer (STOE Stadi P) with Mo $K_{\alpha 1}$ radiation (λ = 0.70932 Å) in transmission geometry using rotating borosilicate capillaries (0.5 mm diameter) in order to avoid surface preferred orientation, a phenomenon often observed for compounds with 2D morphology when the samples are assembled on a flat plate in Bragg-Brentano geometry. Analysis of XRD data was made using FullProf software.

2.4. Chemical characterization

Raman spectroscopy experiments were carried out by a microscope-type HORIBA LabRam Evolution HR with a laser source (λ = 523 nm, 10 mW) from 150 to 800 cm^{-1}. Elemental analysis of pristine and *ex situ* samples was performed through electron dispersive X-ray spectroscopy (EDS) in a Zeiss Supra S5 microscope. On the other hand, the evolution of the oxidation states of the elements upon electrochemical activity was studied through X-ray photoelectron spectroscopy (XPS) measurements. All samples were analyzed using a K-Alpha spectrometer (Thermo Fisher Scientific) equipped with an argon glove box to avoid any air contact, applying a micro-focused, monochromated Al K_α X-ray source (1486.6 eV) with 400 μm spot size. The K-Alpha charge compensation system based on a combination of both electrons and low-energy argon ions was used. Data acquisition and processing were conducted with the Thermo Avantage software. The binding energy was referenced to C 1*s* at 284.4 eV while the overall binding energy scale was controlled using well-known photoelectron peaks of metallic Ag, Au, and Cu.

2.5. Electrochemical experiments

Experiments were carried out in two-electrode Swagelok cells, which were assembled in an argon-filled glovebox (H_2O and $O_2 < 0.1$ ppm). All the parts of the cells were made of materials resistant to the corrosive IL electrolyte: the body and rings were made of Teflon, while the rods were made of tungsten, which is reported to be the least reactive among metals towards the IL electrolyte [55]. The positive electrode was prepared by a slurry mixture in *N*-methylpyrrolidone (NMP, Sigma-Aldrich) consisting of the active material (either VTe_2, $Ti_3C_2T_x$ or the composite $VTe_2/Ti_3C_2T_x$), conductive carbon (C65 Timcal), and polyvinylidene chloride (PVDC) binder (GoodFellow) in an 80:10:10 wt ratio. The slurry was coated onto 12 mm diameter carbon paper disks (Quintech, 120 μm) with a wet thickness of 100 μm. Carbon paper was used as a current collector, since carbon fiber-based materials are inert to electrolyte corrosion, unlike the widely used molybdenum [24,56]. As for the binder, even if PVDC also reacts with the acidic electrolyte like the commonly used PVDF or CMC, the by-products of the reaction are chlorine-based, as the species present in the electrolyte [25]. Using PVDC instead of PVDF prevents the formation of fluorinated species that can interfere with a proper behaviour of the electrolyte [25,57]. Before being introduced into the glovebox, the electrodes were dried at 110 °C for 12 h in a Büchi oven. The mass loading was ~5 mg of composite corresponding to 3.7–4.2 mg of active material (either VTe_2, $Ti_3C_2T_x$ or the composite $VTe_2/Ti_3C_2T_x$) per electrode, that is, ~3.5 mg cm^{-2}. A disk of Al foil (GoodFellow, 0.075 μm, 99 %) served as the negative electrode, and 250 μL of IL mixture of $AlCl_3$:EMImCl (1.5:1 M ratio) as the electrolyte. Two separator disks (Whatman, GF/D) were employed, either untouched or modified with CMK-3 mesoporous carbon. For the preparation of CMK-3 modified separators, a dispersion of CMK-3 mesoporous carbon together with PVDC binder in a weight ratio of 16:1 was prepared in NMP, employing the required amounts to give a concentration of 0.6 mg mL^{-1} in CMK-3. The dispersion was stirred for 30 min and subjected to ultrasonication for 1 h. Vacuum filtration of the dispersion was then carried out using a disk of glass fiber separator as a filter. Once the separator disk was completely covered with a black layer of CMK-3, it was dried at 60 °C for 12 h. Finally, small disks of 12 mm diameter were punched out to be used in the electrochemical cells, with the CMK-3-coated side facing the cathode. The resulting mass loading of CMK-3 is ca. 0.4 mg per separator. The used voltage range for the electrochemical experiments was 2.3–0.3 V. Note that the term 'voltage' is employed instead of 'potential', as for full cells, because metallic aluminum is a real anode used in RABs and 2-electrode cells with no reference electrode have been used in this work [58]. Nevertheless, the specific current and specific capacity values given here are normalized to the mass of the cathodic active material only for the sake of comparison with literature data. The high voltage cutoff is defined by the irreversible oxidation of Cl^- ions of the electrolyte to Cl_2 gas at ca. 2.5 V, while the low voltage cutoff is defined by the plating of aluminum (coming from the reduction of Al^{3+} ions of the electrolyte) on the positive electrode at 0 V. As a standard procedure, galvanostatic experiments were conducted at 100 mA g^{-1} current, while cyclic voltammetry (CV) experiments were performed at 0.2 mV s^{-1}, unless otherwise specified. Galvanostatic intermittent titration technique (GITT) experiments were performed to determine the diffusion coefficient. Each current pulse consisted in applying a current of 100 mA g^{-1} for 5 min. After each current pulse, the system was allowed to reach equilibrium during an open-circuit period until the variation of voltage was less than 1 mV h^{-1}. Concerning the preparation of the charged and discharged *ex situ* electrodes, they were prepared by charging (and subsequently discharging in the case of the discharged samples) at a current of 100 mA g^{-1} to 2.3 and 0.3 V, respectively. After that, the potential was held and the system was allowed to relax and reach equilibrium within 24 h. The electrodes were then removed from the cells inside an argon-filled glovebox and rinsed with 1,2-difluorobenzene, which has been reported as a suitable diluent for IL electrolytes, increasing their fluidity and thus facilitating the removal of excess chloroaluminate electrolyte [59]. The samples were transferred under an argon atmosphere to the microscope/spectrometer, where they were analyzed.

3. Results and discussion

3.1. Structural and morphologic characterization

The dark green powder obtained from the hydrothermal synthesis was confirmed to be VTe_2, as demonstrated by the results of the LeBail fitting of the VTe_2 pattern (Fig. 1a). The crystalline structure of VTe_2 could be successfully indexed with monoclinic space group *C*2/*m*. The fitted lattice parameters are $a = 18.9643(4)$ Å, $b = 3.5677(7)$ Å, $c = 9.0908(9)$ Å and $\beta = 135.1(1)^\circ$, which are in full agreement with those previously reported by Bronsema et al. [60] As for the structure of VTe_2 (Fig. 1a inset), it is arranged in two-dimensional layers consisting of distorted VTe_6 octahedra sharing edges. These octahedra are arranged along the *a* and *b* crystallographic directions, forming sandwich-like layers of Te−V−Te stacked perpendicular to the *c* direction. These layers are held together by Van der Waals forces. A small amount of elemental tellurium (space group $P3_121$) as a minor secondary phase (4.2 %) has been included in the refinement of the VTe_2 pattern (χ^2-factor without including the secondary phase would be increased up to 20.1). Raman spectroscopy (Fig. 1b) was employed to confirm the composition of VTe_2 through the analysis of its characteristic vibrational bands. The Raman signal of the VTe_2 spectrum observed at 138 cm^{-1} is ascribed to the characteristic out-of-plane A_{1g} vibrational band, corresponding to Te atoms vibrating perpendicular to the plane [61]. Besides, other characteristic bands appear (which have been indexed according to other TMCs), such as the E_{1g} mode from the in-plane Te vibration at 190 cm^{-1}; the overlapping E_{2g} and second-order 2LA(M) modes centered at 280 cm^{-1}, and other second-order bands at higher frequencies [62]. The SEM micrograph in Fig. 1c shows the morphology of VTe_2, which appears granular, with particles whose average size is 1–2 μm, although some reach 5 μm, which aggregate to form secondary particles. Elemental analysis (EDS) of the VTe_2 is shown in Fig. 1d and e, evidencing that vanadium and tellurium are evenly distributed in VTe_2, which confirms the success of the hydrothermal synthesis.

3.2. Electrochemical characterization

Electrochemical characterization of VTe_2 was performed by means of cyclic voltammetry (CV) and galvanostatic cycling experiments (Fig. 2a and b). In view of the CV results (Fig. 2a), three main redox processes occur during the charge and discharge of VTe_2. In the first cycle, a reduction peak centered at 1.8 V is observed (R1), followed by a peak at 1.45 V (R2) and a flattened peak at 1.0 V (R3). During the subsequent oxidation scan, the same processes are observed, albeit at displaced voltages due to polarization phenomena. These include O3, O2 and O1 signals. During the second cycle, the CV curve exhibits some changes. In addition to the peaks becoming less intense, which indicates a loss of capacity, peak R2 shifts to lower voltages, now being centered at 1.25 V. However, the corresponding oxidation peaks are still present, and the following cycle shows a similar behavior. These results point to an activation process during the initial cycle, after which the reduction/oxidation process becomes reversible [63]. According to the literature, O3 and R3 peaks correspond to the Te^0/Te^{2-} redox pair, O2 and R2 to Te^{2+}/Te^0, and O1 and R1 to both V^{5+}/V^{4+} and Te^{4+}/Te^{2+} redox pairs, although they are indistinguishable due to the close voltage value of both redox pairs [64]. Fig. 2b shows the galvanostatic curves corresponding to the first three cycles of VTe_2 at 100 mA g^{-1} specific current. The three electrochemical processes determined by CV during (dis)charge are reflected as voltage plateaus in the galvanostatic profile, located at consistent voltage values. A notable capacity decrease can be observed, with a reduction of approximately 60 % in discharge capacity after the first cycle, from 275 to 107 mAh g^{-1}, and a further decrease to 56 mAh g^{-1} by the third cycle. Such decay can be attributed to the dissolution of the active material during oxidation and the subsequent shuttle effect of the soluble species migrating towards the anode, resulting in a loss of active material from the cathode [65]. Another possible reason for the capacity loss is the formation of a cathode-electrolyte interphase (CEI) layer on the cathode during the initial cycles [66]. These phenomena also impact the coulombic efficiency, especially in the first cycle. At this point, it is important to note that the $VTe_2/Ti_3C_2T_x$ composite, whose enhanced electrochemical

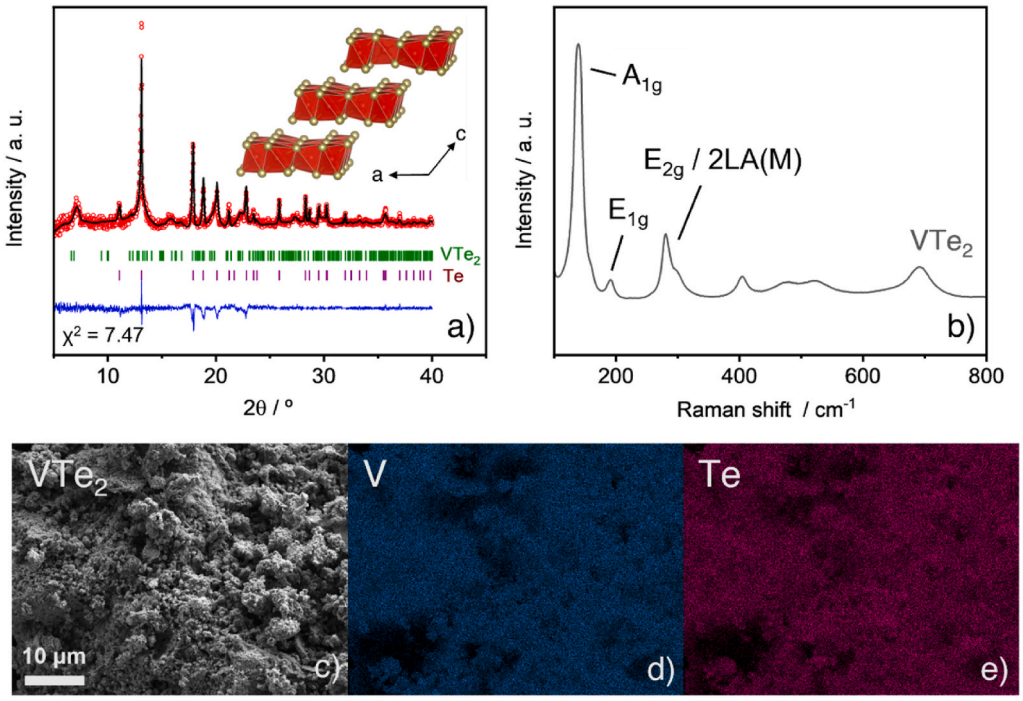

Fig. 1. a) LeBail fitting of the XRD pattern of $VTe_2/Ti_3C_2T_x$ composite. Red circles: experimental pattern; black solid line: calculated pattern; bottom blue line: difference between experimental and calculated patterns; vertical bars: position of Bragg reflections (green: VTe_2, purple: Te). Inset: projection of the structure of VTe_2 along *b* axis; VTe_6: red octahedra, Te: gold spheres; b) Raman spectrum of VTe_2, c) SEM micrograph of VTe_2 and the corresponding EDS of V (d) and Te (e).

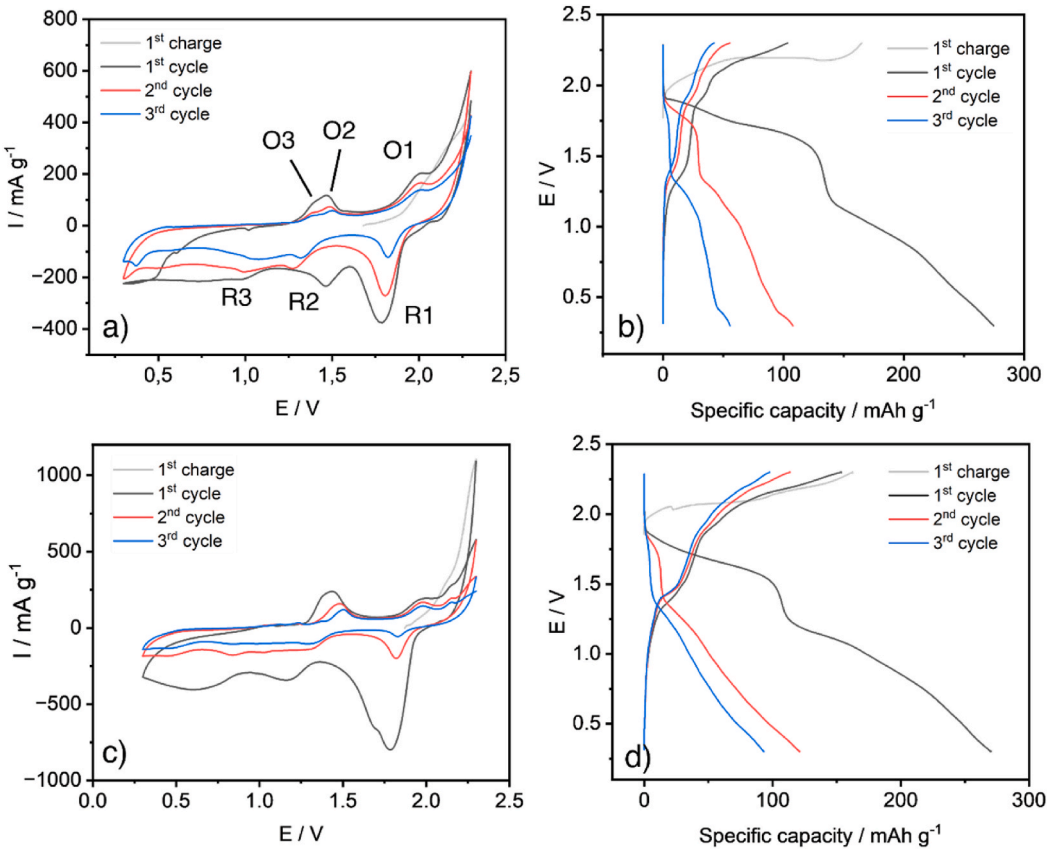

Fig. 2. Three first cycles of a) cyclic voltammetry at 0.5 mV s^{-1} scan rate and b) charge/discharge profile at 100 mA g^{-1} of VTe_2 vs. Al anode. Three first cycles of c) cyclic voltammetry at 0.5 mV s^{-1} scan rate and d) charge/discharge profile at 100 mA g^{-1} of the $VTe_2/Ti_3C_2T_x$ composite vs. Al anode.

performance over as-prepared VTe_2 will be discussed below, experiences the same redox reactions as those observed in Fig. 2a and b, in view of the identical CV and galvanostatic curves (Fig. 2c and d). This finding, together with the lack of significant peaks in the CV profile of $Ti_3C_2T_x$ (Fig. S1a), confirms that the electrochemically active species in the composite is VTe_2. Interestingly, $Ti_3C_2T_x$ does not exhibit substantial electrochemical activity, despite its high specific capacity during the first oxidation, which decreases rapidly in the subsequent cycles, evidencing its irreversibility (Fig. S1b).

3.3. *Characterization of $VTe_2/Ti_3C_2T_x$ composite*

$VTe_2/Ti_3C_2T_x$ composite was characterized to prove the suitability of the employed synthesis route and the validity of the results presented in the following section. Fig. 3a compares the XRD patterns of as-prepared VTe_2, $Ti_3C_2T_x$ and $VTe_2/Ti_3C_2T_x$ composite. As for VTe_2, the synthesis of $VTe_2/Ti_3C_2T_x$ composite yields a small amount of impurities of Te (4.2 %), while as for $Ti_3C_2T_x$, some TiO_2 (anatase) has been detected, coming from the surface oxidation of the MXene. In the case of $VTe_2/Ti_3C_2T_x$, reflections coming from both compounds appear, although only the (002), (106) and (110) reflections of $Ti_3C_2T_x$ are observed due to its lower amount in the composite. The XRD pattern of $Ti_3C_2T_x$ shows the typical (00*l*) reflections ascribed to the *c* lattice parameter at low angles ($2\theta < 15°$) and higher order reflections at high angles ($2\theta > 15°$). From the 2θ value of the (00*l*) reflections, it is possible to determine the interlayer spacing of $Ti_3C_2T_x$, 10.06 Å, which is consistent with previous reports [67]. Raman spectra of VTe_2, $Ti_3C_2T_x$ and $VTe_2/Ti_3C_2T_x$ composite are shown in Fig. 3b. In the case of the $Ti_3C_2T_x$, the spectrum shows its characteristic profile, divided into three distinct regions: the low-frequency region corresponding to the vibration of the whole layers (Ti, C, and T_x), with the most intense signal, the A_{1g} vibration band, at 203 cm^{-1}; vibrations in the 250–500 cm^{-1} frequency range related to surface terminal groups, and high-frequency vibrations ascribed to carbon and terminal groups (C, T_x) [68]. The Raman spectrum of $VTe_2/Ti_3C_2T_x$ exhibits similar vibrational bands to those of VTe_2, confirming the presence of VTe_2 in the composite. In addition, some amount of $Ti_3C_2T_x$ was detected in the composite, since several characteristic bands of MXenes were observed in the spectrum of $VTe_2/Ti_3C_2T_x$, especially the most intense band A_{1g} at 203 cm^{-1}. The morphology of the studied compounds was analyzed by SEM micrographs (Fig. 3c–e). $Ti_3C_2T_x$ exhibits the 2D layered morphology characteristic of MXenes: on the one hand, the plane surface has some rough areas and defects, and on the other hand, the side section evidences the restacking of the $Ti_3C_2T_x$ sheets (Fig. 3d). Concerning the $VTe_2/Ti_3C_2T_x$ composite, it shows morphological features of both $Ti_3C_2T_x$ and VTe_2: particles consisting of stacked layers can be observed, with different lengths and widths but a consistent thickness of 5–6 μm, while smaller particles of about 1 μm are attached to the surface of the layered particles and even embedded in between their sheets (Fig. 3e); elemental analysis results shown below also evidence that VTe_2 is actually covering the entirety of the surface of the MXene layers. As previously confirmed by XRD results, SEM images demonstrate the close contact between VTe_2 and $Ti_3C_2T_x$ in the composite. Elemental analysis (EDS) of the three samples is shown in Fig. S2. Titanium and carbon are evenly distributed in $Ti_3C_2T_x$. In addition, an intense signal corresponding to oxygen and fluorine has been observed, originating from the T_x terminal groups, such as −O−, −OH, and −F, derived from the synthesis of the MXene. In the case of $VTe_2/Ti_3C_2T_x$ composite, the four main elements exhibit a homogeneous distribution. Based on the ratio between V and Ti elements, the $VTe_2/Ti_3C_2T_x$ composite was determined to be 87.8 at% VTe_2 and 12.2 at% $Ti_3C_2T_x$.

As discussed in the previous section, VTe_2 suffers a drastic capacity

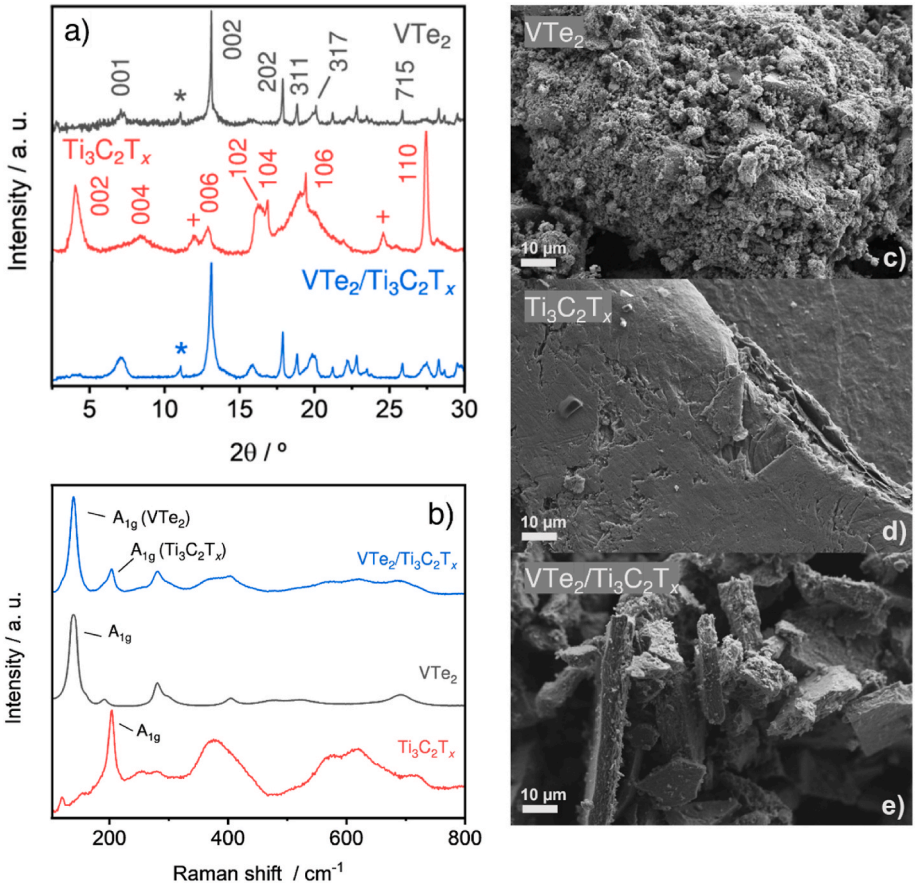

Fig. 3. a) Selected angular region of XRD patterns of VTe_2, $Ti_3C_2T_x$ and $VTe_2/Ti_3C_2T_x$ composite. Selected reflections are indexed. Reflections from Te (*) and TiO_2 anatase (+) are marked; b) Raman spectra of VTe_2, $Ti_3C_2T_x$ and $VTe_2/Ti_3C_2T_x$ composite; SEM micrographs of c) VTe_2, d) $Ti_3C_2T_x$ and e) $VTe_2/Ti_3C_2T_x$ composite.

drop already in the initial cycles (Fig. 2b), which is associated with side reactions between the cathode and the chloroaluminate electrolyte, leading to the dissolution of the active material and the subsequent shuttling of the soluble species towards the anode through the separator. Fig. 4a shows that the decay of capacity keeps going during the following cycles, delivering a poor cycling performance, barely completing 75 cycles and with an almost total loss of capacity (<10 mAh g^{-1}) at that point. $VTe_2/Ti_3C_2T_x$ composite delivers a better cyclability (>300 cycles), although the capacity stabilizes at only 18 mAh g^{-1}, with a coulombic efficiency of 95 %. Interestingly, pure MXene delivers a similar capacity value (17 mAh g^{-1}) at cycle 300 under the same current density, evidencing the total dissolution of VTe_2 present in the $VTe_2/Ti_3C_2T_x$ composite. In view of these results and considering the 87.8:12.2 atomic ratio of the $VTe_2/Ti_3C_2T_x$ composite obtained by EDS analysis, the MXene can be considered an additive compound that enhances the electrical properties of the active material, as deduced from the comparison of the electrochemical performance in terms of capacity retention and cycle life of VTe_2 and $VTe_2/Ti_3C_2T_x$. In addition, $Ti_3C_2T_x$ prevents the shuttle effect of the soluble species originating from the cathodic active material, dissolved by the corrosive electrolyte, at least for a certain number of cycles. Fig. 4b shows the performance of the studied compounds at different current densities. A comparison of these results with the constant current experiments (Fig. 4a) allows us to draw two main conclusions. Firstly, VTe_2 does not experience a cell failure as

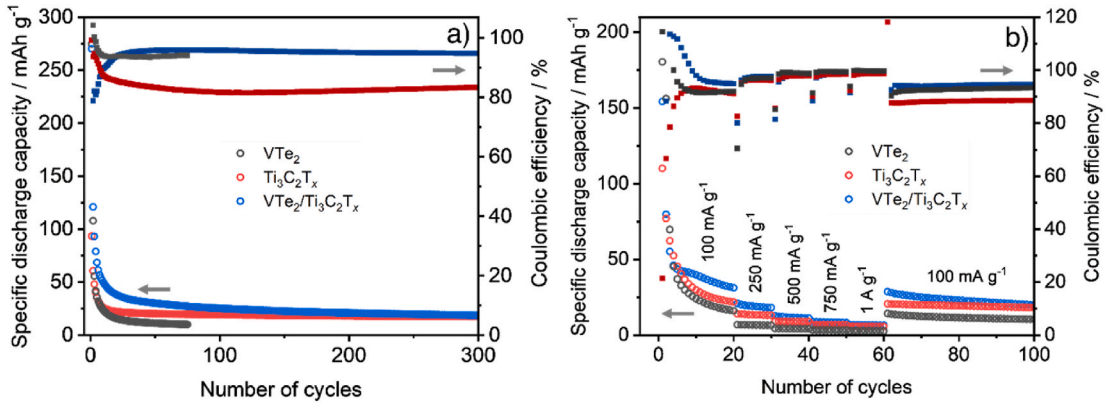

Fig. 4. a) Evolution of specific discharge capacity versus the number of cycles at 100 mA g^{-1} current density and b) Rate capability at different current densities of VTe_2, $Ti_3C_2T_x$ and $VTe_2/Ti_3C_2T_x$ composite vs. Al anode.

it did after 70 cycles in the constant current experiment (Fig. 4a). This behavior can be explained by the fact that the higher the applied current, the faster the charge and discharge steps will be completed. During the oxidation process, soluble species generated from the dissolution of cathodic active materials are produced. Conversely, during the reduction reaction, these species are transformed back into non-soluble compounds, assuming they remain at the cathode side of the cell and there are no shuttle effect phenomena. If the oxidation and reduction processes occur rapidly enough due to a high applied current, the soluble active species do not have sufficient time to migrate through the separators towards the anode, preventing the loss of active material from the cathode and leading to a stabilization of the cell performance. Secondly, in the case of the influence of the MXene on the electrochemical performance, which is studied by comparing the results of VTe_2 and $VTe_2/Ti_3C_2T_x$, it has the same effect as in the constant current galvanostatic cycling (Fig. 4a): acting like an additive compound, the amount of MXene present in the composite leads to an improvement of the electrical properties, which is reflected in the better cyclability of the $VTe_2/Ti_3C_2T_x$ composite with respect to VTe_2. Nevertheless, the dissolution and shuttling of the active material is still an issue, considering the low capacity. This problematic issue will be addressed in the next section with CMK-3 modified separators.

3.4. Stability optimization via CMK-3 modified separator

In order to retain the soluble species at the cathode side and improve the electrochemical performance of $VTe_2/Ti_3C_2T_x$ composite (Fig. 4), a CMK-3 modified separator was employed. The uniformity of the coating of CMK-3 on the surface of the separators has been demonstrated by the SEM cross-section images (Fig. S3). Fig. 5a shows the cycling performance of a cell bearing a $VTe_2/Ti_3C_2T_x$ composite cathode and CMK-3 modified separators. Even if there is still a significant capacity decay during the first five cycles, the value tends to stabilize afterward, with $VTe_2/Ti_3C_2T_x$ delivering an acceptable capacity of 63 mAh g^{-1} at cycle 300, which represents a 3.5-fold increase in the capacity value obtained with conventional separators (Fig. 4a). Such results evidence a synergistic effect of $Ti_3C_2T_x$ and the CMK-3 modified separators that entail an improvement of the capacity retention of VTe_2. The CV and galvanostatic cycling results of $VTe_2/Ti_3C_2T_x$ with CMK-3 modified separators (Fig. S4) show similar behavior to those obtained from cells of $VTe_2/Ti_3C_2T_x$ with conventional separators (Fig. 2c and d). In addition, the CV of a cell bearing a blank electrode without active material and CMK-3 separators shows no significant peaks (Fig. S5). Both findings demonstrate that the improvement in the capacity retention of the $VTe_2/Ti_3C_2T_x$ composite is due to the modified separators preventing the migration of the soluble active species to the anode, thereby discarding any electrochemical activity that these separators may have and leaving VTe_2 as the only active species in the system. It is important to note that the CV shown in Fig. S5 also demonstrates the suitability of carbon paper as current collector, discarding any possible reactions with the chloroaluminate electrolyte even under electrochemical activity. Several reports have already demonstrated the ability of CMK-3 modified separators to retain soluble species on the cathode side of the cell, not only in chalcogen-based RABs [52,69] but also in other battery systems such as Li-S [70]. In this work, we have further proven this beneficial property of the modified separators through *ex situ* elemental analysis experiments, focusing on the amount of Te on the aluminum anode, as this is the only element present in the cathode that forms soluble species capable of migrating through the separator towards the anode. Fig. S6 compares the aluminum anode of a $VTe_2/Ti_3C_2T_x$ cell with modified separators and a $VTe_2/Ti_3C_2T_x$ cell with conventional, unmodified separators. Both electrodes were removed from the cell in the charged state to ensure the maximum amount of soluble species in the system. In the case of the anode from the cell with modified separators, the amount of Te in the anode is significantly lower than when the conventional separators were used, confirming that the CMK-3 modified separators are suitable for retaining the tellurium-based soluble species in the cathode. However, the fluctuating behavior of the coulombic efficiency (Fig. 5a) suggests that shuttle effect phenomena may still occur (although parasitic reactions in the electrolyte cannot be discarded): given the smooth variation of the discharge capacity, the fluctuations in the coulombic efficiency originate from the charge process, that is, oxidation. Considering that soluble species are generated upon oxidation [48–51], it can be concluded that a certain amount of the active species still migrate towards the anode through the separators. Our group is currently working on optimize the procedure for modifying the separators in order to mitigate the shuttle effect of soluble species. In any case, the coulombic efficiency and discharge capacity values eventually become stable. Such capacity value, together with the high voltage of the electrochemical processes of VTe_2 (with the main plateau located at 1.8 V, second only to graphitic materials [71]), makes this compound an appealing cathode material for aluminum batteries. For comparison, Table S1 shows the electrochemical performance of other reported cathodes for RABs. Employing CMK-3 modified separators also contributes to the improvement of the electrochemical performance at high rates (Fig. 5b). By using modified separators, the specific capacity delivered by the $VTe_2/Ti_3C_2T_x$ composite increases from 31 to 75 mAh g^{-1} at 100 mA g^{-1}, from 18 to 50 mAh g^{-1} at 250 mA g^{-1}, from 11 to 38 mAh g^{-1} at 500 mA g^{-1}, from 8 to 33 mAh g^{-1} at 750 mA g^{-1} and from 7 to 31 mAh g^{-1} at 1 A g^{-1} (compare Fig. 4b and 5b). Both cells show good capacity retention considering the value of capacity after coming back to the initial specific current of 100 mA g^{-1}. The fluctuating behavior of the coulombic efficiency of the $VTe_2/Ti_3C_2T_x$ composite is not observed in this experiment. As in the case of $VTe_2/Ti_3C_2T_x$ composite with conventional separators (Fig. 4b), if the applied current is high enough, it can mitigate the shuttle effect of the soluble active species. In addition,

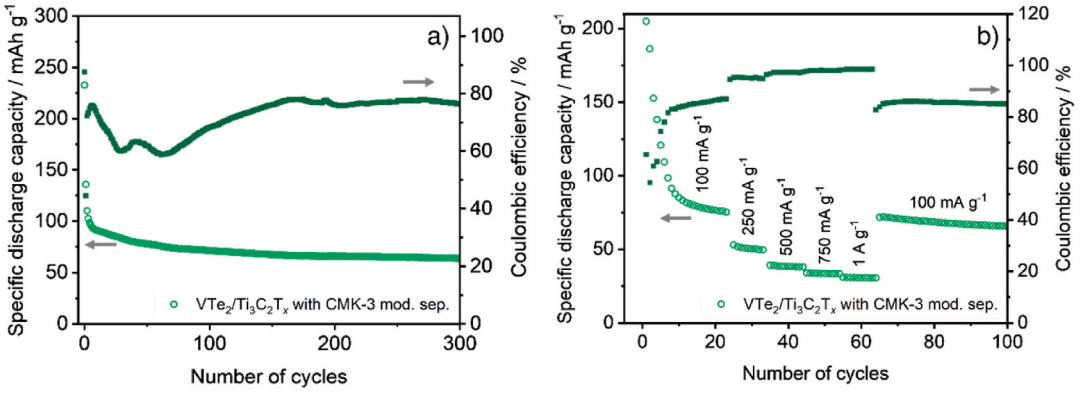

Fig. 5. a) Evolution of specific discharge capacity versus the number of cycles at 100 mA g^{-1} current density and b) Rate capability at different current densities of $VTe_2/Ti_3C_2T_x$ composite with CMK-3 modified separators vs. Al anode.

the hypothetical parasitic reactions in the electrolyte are avoided at high current values, as their kinetics are usually slower.

3.5. Analysis of the charge storage mechanism

The experiments conducted to determine and analyze the storage mechanism on VTe_2 were performed on the $VTe_2/Ti_3C_2T_x$ composite due to its better stability towards the corrosive electrolyte (as concluded from a better capacity retention than as-prepared VTe_2, see Fig. 4) while preserving the same redox chemistry as the as-prepared VTe_2, as demonstrated in Fig. 2. In RABs, the charge transport of cathode materials can be fundamentally classified into two main categories: $AlCl_4^-$ anions or Al^{3+} cations as hosted ions [72]. To determine which mechanism takes place in VTe_2, we performed *ex situ* elemental analysis of the electrodes (Fig. 6). EDS mapping of the charged electrode (Fig. 6a) shows that both Al and Cl are present in significant amounts compared to the discharged electrode (Fig. 6b), indicating that the charge transport within VTe_2 is based on $AlCl_4^-$ anions. Note that, in the case of the dual-ion mechanism, the anionic species are inserted in the cathode during charging and leave during discharging. The mapping of V is included to show the correlation between the location of the observed Al and Cl and the particles of the VTe_2, indicating an electrochemical interaction of chloroaluminate species with the active material. In addition, this approach allows the electrochemically active Cl^- of the chloroaluminate species to be distinguished from the inactive Cl^- of the PVDC binder, which is visualized as a "cloud" covering the entire image area. Even if the electrodes were rinsed with 1,2-difluorobenzene to remove the electrolyte, some residual amount can remain adsorbed to the electrode, explaining the presence of Al and Cl in the discharged electrode. Other work has also proposed that these additional amounts of Al and Cl might come from a CEI layer formed during the first cycles [66]. In any case, a mechanism based on Al^{3+} cations can be excluded, since this would imply an increase in Al in the discharged electrode, whereas the EDS mapping shows an evident decrease in Al after discharge.

Changes in the oxidation state of the different elements constituting the cathode active material upon electrochemical activity were studied by *ex situ* XPS, which unveils the redox mechanism of VTe_2 as cathode for RABs (Fig. 7). The clear O 1*s* signal at 530.3 eV stems from the oxidized species of the different metals (V−O, Te−O and Ti−O) and is accompanied by two further peaks at 531.6 and 533.0 eV corresponding to C=O and C−O species, respectively, mainly originating from the contamination commonly observed during air handling of the pristine samples. In the case of vanadium, the V 2*p* doublets reveal binding energies corresponding to V^{5+} (V $2p_{3/2}$ at 517.3 eV) and V^{4+} (V $2p_{3/2}$ at 516.0 eV) oxidation states [73]. In the pristine electrode, it can be observed that the main contribution stems from V^{5+} and not from the expected V^{4+} oxidation state, which was attributed to surface oxidation phenomena, given the high stability of V^{5+} oxidation state compared to V^{4+}. After charging up to 2.3 V, a 1:1 ratio between V^{5+} and V^{4+} is observed, whereas the discharged electrode down to 0.3 V shows a dominant contribution of V^{4+}, indicating that almost all the V^{5+} of the charged sample has been reduced upon discharge. On the other hand, a total (or quasi-total) oxidation of V^{4+} to V^{5+} is not observed, probably because the electrode has not reached a thermodynamic equilibrium state during the electrochemical charge. Concerning the discharged electrode down to 0.3 V, the dominant contribution is now from V^{4+}, indicating that almost all the V^{5+} of the charged sample has been reduced upon discharge. These results, despite surface oxidation perturbations, demonstrate that the redox pair V^{5+}/V^{4+} plays a role in the electrochemical activity of VTe_2. Te 3*d* spectra are shown in Fig. 7b. Two doublets can be distinguished corresponding to two different oxidation states: one with Te $3d_{5/2}$ at 573.0 eV attributed to Te^{2-} and a second one at 576.5 eV attributed to Te^{4+} states [74]. Again, as in the case of vanadium, a surface oxidation is observed for the pristine sample with a main Te^{4+} peak and a weaker Te^{2-} signal. When the electrode is charged up to 2.3 V, the Te^{2-} peak disappears and its concentration is under the detection limit, which indicates that a total (or quasi-total) oxidation to Te^{4+} occurs. Subsequently, after discharging the electrode down to 0.3 V, the Te^{2-} peak is observed again with a high intensity, while the Te^{4+} peak almost disappears, evidencing the quasi-total reduction of Te^{4+} back to Te^{2-} upon discharge. XPS experiments have thus demonstrated that both vanadium and tellurium are involved in the electrochemical activity of VTe_2 through the redox pairs V^{5+}/V^{4+} and Te^{4+}/Te^{2-}. Titanium from the MXene present in the $VTe_2/Ti_3C_2T_x$ composite was also analyzed by *ex situ* XPS experiments (Fig. S7). It must be noted that the signals are weak and noisy due to the low concentration of Ti. Nevertheless, the spectra could be deconvoluted into two doublets, attributed to Ti^{4+} (458.5 eV) and Ti^{3+} (455.6 eV) oxidation states [75]. Whereas Ti^{3+} is one of the several oxidation states that titanium exhibits in $Ti_3C_2T_x$, Ti^{4+} has been attributed to surface oxidation, due to Ti^{4+} being the most stable among the cations of titanium. Most importantly, no changes are observed in the Ti 2*p* spectrum upon electrochemical activity, which indicates that Ti does not participate in the electrochemical activity of the $VTe_2/Ti_3C_2T_x$ composite. These results demonstrate that $Ti_3C_2T_x$ is not electrochemically

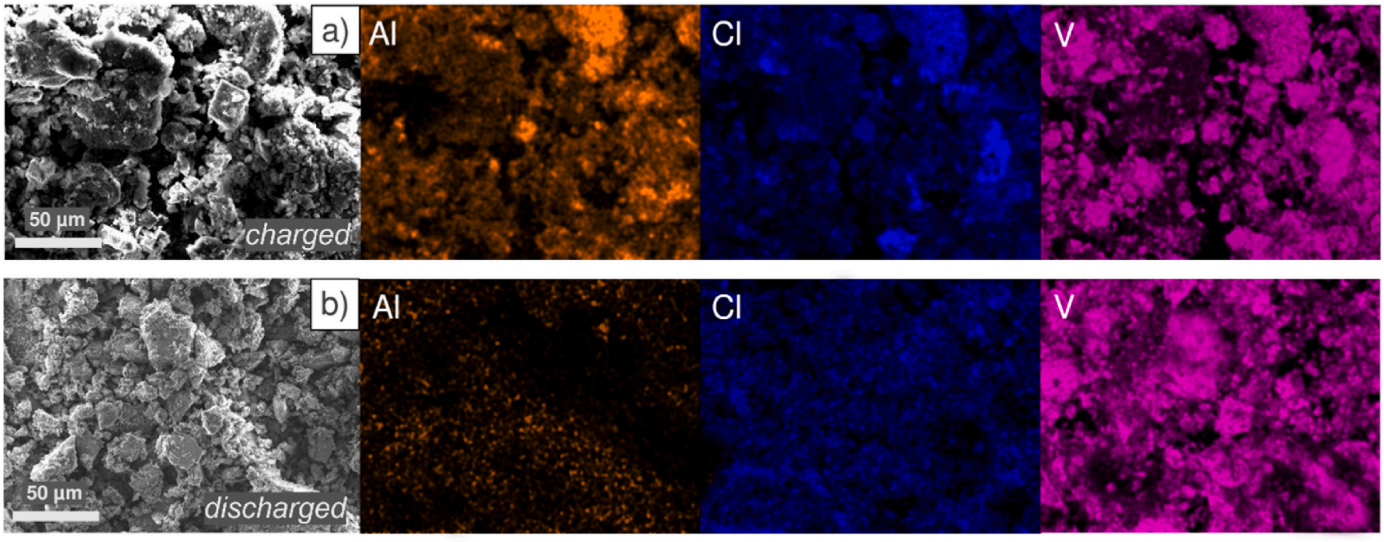

Fig. 6. SEM micrographs and EDS mapping of Al, Cl and V of *ex situ* $VTe_2/Ti_3C_2T_x$ electrodes after a) charge (2.3 V) and b) discharge (0.3 V).

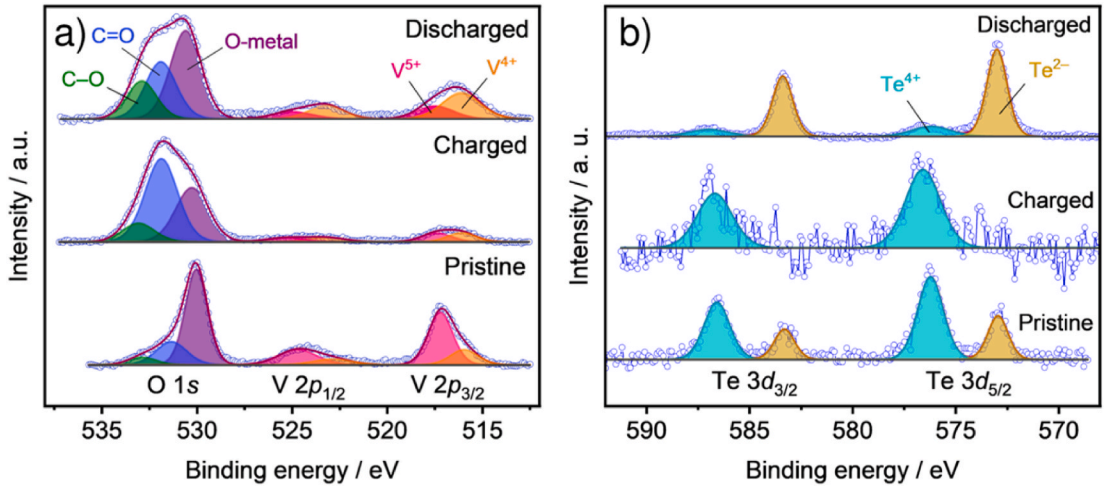

Fig. 7. High-resolution XPS of a) O 1*s* and V 2*p* and b) Te 3*d* of $VTe_2/Ti_3C_2T_x$ electrodes at pristine, charged and discharged states.

active and that VTe_2 is the only active species in the composite, with the MXene acting as an additive compound that enhances the electrochemical properties of VTe_2, as previously proven by the electrochemical experiments upon $Ti_3C_2T_x$ (Fig. S1).

In addition, the trend of the amounts of Al and Cl observed in the XPS results confirm that the charge storage mechanism is based on $AlCl_4^-$ anions, in agreement with the results obtained through EDS elemental analysis (Fig. 6). It should be noted that an N 1*s* peak at 402.0 eV is observed on both charged and discharged electrodes. This signal is attributed to residual EMImCl salt from the electrolyte, which cannot be rinsed even with 1,2-difluorobenzene [25]. The atomic percentage of Cl coming from the salt was determined from the amount of N. In addition, "covalent" Cl coming from the PVDC binder can be distinguished, since its signal appears at 200.5 eV, whereas the signal of "ionic" Cl from chloroaluminate species is located at 198.9 eV. Taking these considerations into account, the atomic percentages of Al (3+, 74.9 eV) and Cl (1–, 198.9 eV) coming from the electrochemical interaction of chloroaluminate species with cathode (*i.e.* discarding the contributions from residual electrolyte and binder) are 7.5 at% and 3.3 at% for the charged electrode and 3.7 at% and 1.7 at% for the discharged electrode, respectively. It can be observed that the charged sample is rich in Al^{3+} and Cl^- while the amount of these elements in the discharged sample is lower, although both are still present in the discharged sample. Even if the ratio between both elements is not as expected, this behavior can be explained by the fact that $AlCl_4^-$, as an anion, goes into the cathode during charging and leaves the cathode during discharging. In any case, a mechanism based on Al^{3+} cations can be discarded, as it would entail an insertion of Al^{3+} during the discharge process, whereas the XPS results show a clear decrease in the atomic percentage of Al in the discharged electrode compared to the charged one. The residual amount of Al and Cl in the discharged electrode could be due to the remaining chloroaluminate electrolyte that has not been rinsed, or due to a lack of equilibrium conditions during the electrochemical preparation of the electrode.

In order to further analyze the species formed upon charge and discharge, we performed *ex situ* XRD. Fig. S8 compares the XRD patterns of charged and discharged electrodes of $VTe_2/Ti_3C_2T_x$, including the pattern of pristine $VTe_2/Ti_3C_2T_x$ as a reference. The XRD pattern of the electrode charged up to 2.3 V evidences the formation of $TeCl_3AlCl_4$, which is the species that Te^{4+} forms in chloroaluminate ionic liquids [50,51]. The charged electrode also shows some remaining amount of VTe_2 that has not been oxidized. After discharging down to 0.3 V, VTe_2 is again formed upon reduction of Te^{4+} to Te^{2-}. In addition, the impurities of Te present in the pristine sample are no longer observed due to a total reduction of Te, although some amount of $TeCl_3AlCl_4$ formed upon charging is present. The *ex situ* XRD analysis confirms the results of the XPS experiments, demonstrating that the Te^{4+}/Te^{2-} redox pair participates in the electrochemical activity of VTe_2 and that the redox reactions involved are fully reversible. In addition, VTe_2 powder was soaked in the chloroaluminate electrolyte to check if this compound undergoes chemical changes besides electrochemical changes. The angular position of the reflections from the XRD patterns (Fig. S9) before and after the treatment shows no changes, indicating that the electrolyte reacts with VTe_2 only upon electrochemical activity, specifically upon oxidation. However, a broadening of the reflections is observed, which indicates the loss of crystallinity of VTe_2 upon contact with the electrolyte. In addition, the separator of an open cell after operation exhibits a yellowish color (Fig. S10), coming from the vanadium and/or tellur-chlorine complexes (the electrolyte is originally colorless), which evidences the dissolution of the cathode.

Considering the results obtained through *ex situ* XRD and XPS experiments, it is possible to describe the reactions that VTe_2 experiences as a cathode for RABs. First, during the synthesis, pristine VTe_2 undergoes surface oxidation (Eq. (2)), which affects the oxidation state of V and Te, producing elemental Te (as observed in the XRD pattern in Fig. 1) and V_2O_5 (as demonstrated by the observed V^{5+} in the XPS results of Fig. 7a) in a minor amount according to the stoichiometry, which would explain the absence of V_2O_5 in the XRD pattern. In addition, XPS reveals the presence of Te^{4+} in the pristine sample (Fig. 7b), which may come from further oxidation of Te to TeO_2 (Eq. (3)).

$$4\,VTe_2 + 5\,O_2 \rightarrow 8\,Te + 2\,V_2O_5 \qquad \text{Eq. 2}$$

$$Te + O_2 \rightarrow TeO_2 \qquad \text{Eq. 3}$$

Regarding the electrochemical reaction, both V and Te are involved in the redox reaction as demonstrated by the *ex situ* XPS experiments (Fig. 7). In the case of vanadium, V^{4+} from VTe_2 is oxidized to V^{5+} upon charge, which forms the complex species VCl_6^- in chloroaluminate IL environments [76]. On the other hand, the tellurium oxidation state increases from Te^{2-} in VTe_2 to Te^{4+} in $TeCl_3AlCl_4$, which is the complex that Te^{4+} ions form in the $AlCl_3$-EMImCl electrolyte [50,51]. Note that the presence of $TeCl_3AlCl_4$ upon charge was proven by *ex situ* XRD studies (Fig. S8). As mentioned in the Introduction, $TeCl_3AlCl_4$ is soluble in the electrolyte and can migrate through the separator to the anode. Therefore, the proposed electrochemical reaction (Eq. (4)) that the cathode experiences during charge can be expressed as follows:

$$n\,VTe_{2(s)} + 12n\,Cl^-_{(sol)} + 2n\,AlCl^-_{4(sol)} \rightarrow 2n\,TeCl_3AlCl_{4(sol)} + n\,VCl^-_{6(sol)} + 13n\,e^-$$ Eq. 4

Concerning the anode, the plating of Al takes place through the reduction of $Al_2Cl_7^-$ species upon charging the cell (Eq. (5)), generating the $AlCl_4^-$ ions that react with the cathode in Eq. (4).

$$Al_2Cl_7^- + 3\,e^- \rightarrow Al + AlCl_4^- + 3Cl^-$$ Eq. 5

3.6. Kinetics analysis of charge storage

To further understand the charge storage mechanism of VTe_2 as a cathode for RABs, CV was applied from 0.5 to 2.5 mV s^{-1} (Fig. 8a). In order to ensure that the evolution of the peaks and the area enclosed by the CV curves was only dependent on the scan rate, the cell was initially subjected to several conditioning cycles at 0.5 mV s^{-1}. Once the CV cycles were stable, three cycles per scan rate (in increasing order) were performed. The CV profile remains similar at each scan rate (Fig. 8a), although more intense signals and greater polarization can be observed as the scan rate increases. In addition, the shape of the CV profile becomes more rectangular, indicating an increase in the contribution of the surface-controlled, capacitive processes to the charge storage mechanism [77]. In order to determine the diffusive or capacitive behavior of each redox process of VTe_2, the following formula was employed [78]:

$$I = a\nu^b$$ Eq. 6

where I is the current at the peak maximum, ν is the scan rate, and a and b are adjustable parameters. The value of b oscillates between 0.5 (corresponding to a pure diffusion-controlled process) and 1 (indicative of a pure surface-controlled process without diffusion limitations) [79,80]. The calculation of the b-value is made through Eq. (7) in logarithmic form:

$$\lg I = \lg a + b \lg \nu$$ Eq. 7

In a $lg\ I$ vs $lg\ \nu$ plot, the slope corresponds to the b-value (Fig. 8b). Redox processes at low voltages, peaks R3 and O3, are highly surface-controlled, in view of their high b-values. Moving on to processes at intermediate voltages, peaks R2 and O2, the contribution of the diffusion mechanism increases while the contribution of the surface mechanism is still significant. At high voltages, peaks R1 and O1 exhibit the lowest b-values, closer to 0.5, indicating that the diffusion contribution dominates the charge storage mechanism corresponding to these processes. This versatility of the charge storage mechanism depending on the voltage demonstrates that the entry of $AlCl_4^-$ ions into the cathode (which occurs during charging and thus, reaching its maximum at high voltages), enhances the diffusion of the ions themselves. Such behavior is likely due to $AlCl_4^-$ ions expanding the diffusion paths of the VTe_2 and decreasing the diffusion energy barrier for the incoming $AlCl_4^-$ ions. However, during discharge, *i.e.*, when moving towards low voltages, $AlCl_4^-$ ions leave the cathode and the diffusion process becomes hindered, as evidenced by the b-values at low voltage.

On the other hand, the CV profiles at each scan rate were deconvoluted into diffusion and surface contributions, thus obtaining the ratio between both mechanisms along the whole voltage range, not only at the voltage corresponding to the peaks, as in the case of the previous procedure. In order to determine the ratio, Eq. (6) can be rewritten as:

$$I = k_1\nu + k_2\nu^{0.5}$$ Eq. 8

where $k_1\nu$ is the current originating from the surface-controlled mechanism and $k_2\nu^{0.5}$ is the current originating from the diffusion-controlled

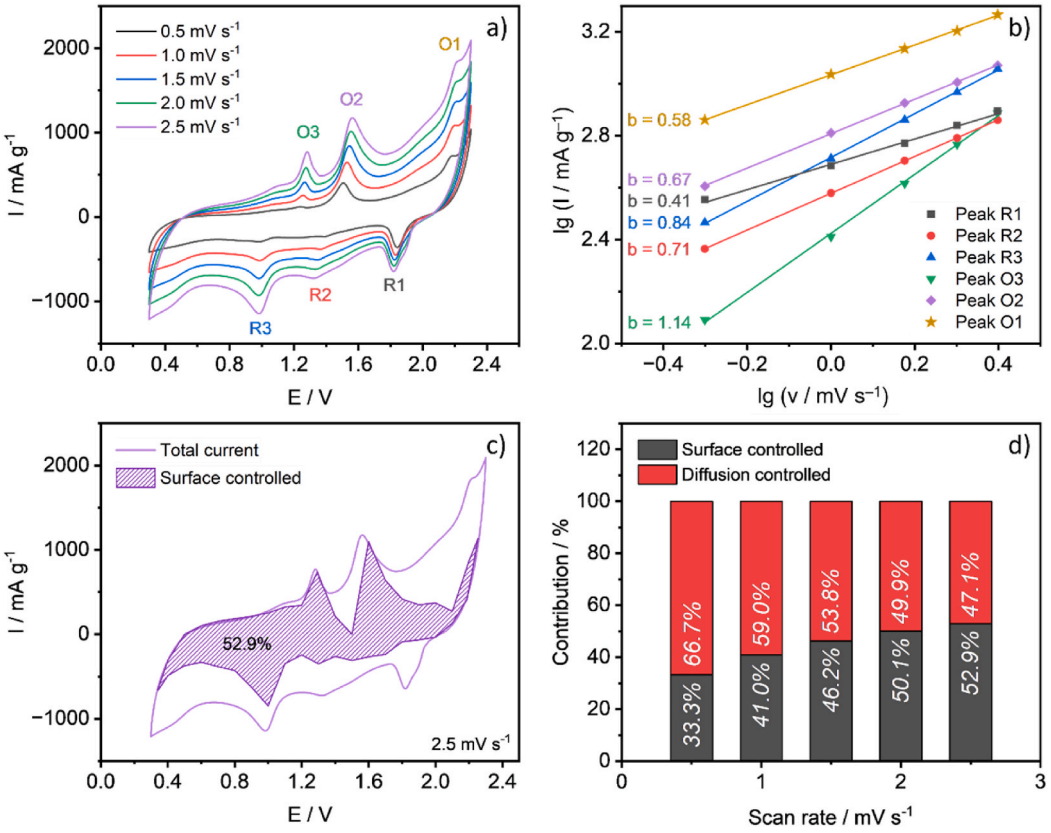

Fig. 8. a) CV profiles of $VTe_2/Ti_3C_2T_x$ at different rates; b) graphical determination of the b-value for each CV peak; c) CV profile of $VTe_2/Ti_3C_2T_x$ at 2.5 mV s^{-1}, the shaded area corresponds to the current contribution of the surface-controlled processes to the total current; d) Ratio between surface-controlled and diffusion-controlled processes at several scan rates.

mechanism (note that the exponents, which correspond to the *b*-value of Eqs. (6) and (7), are 1 and 0.5, respectively). By rearranging and performing a linear fitting of Eq. (8), the parameters k_1 and k_2 were obtained at each voltage value along the 2.3–0.3 V voltage range, providing the ratio between the contribution of diffusion-controlled and surface-controlled processes as a function of voltage. Fig. 8c visually shows the ratio between both contributions at 2.5 mV s^{-1}. At this rate, capacitive processes provide 52.9 % of the current signal from VTe_2. In addition, their contribution is more significant at low voltages than at high voltages, in good agreement with the *b*-values obtained in Fig. 8b. Fig. 8d shows the ratio between the contributions at each scan rate. At 0.5 mV s^{-1}, the diffusion-controlled processes dominate the mechanism (66.7 %), although the surface-controlled processes exhibit a significant contribution (33.3 %). As the scan rate increases, the contribution of capacitive processes to the charge storage mechanism becomes progressively higher, up to 52.9 % at 2.5 mV s^{-1}. Interestingly, none of the mechanisms completely dominates at any scan rate when considering the whole voltage range, indicating the versatility of the charge storage mechanism of VTe_2 composite, which was previously demonstrated by Fig. 8b and c.

In order to gain more insight into the kinetics of the diffusion of $AlCl_4^-$ ions, GITT experiments were carried out. Fig. S11a shows the galvanostatic discharge at quasi-equilibrium conditions, along with the voltage changes upon current pulses and relaxations versus time. Both processes at 1.8 V and 1.2 V (previously observed in Fig. 2) are present, although the process at 0.6 V is not observed here due to voltage limitations: as a full cell, the cell polarity would be inverted below 0 V, therefore the discharge pulses cannot discharge the cell further from this point, resulting in a "false" plateau at 1.2 V in the quasi-equilibrium curve. It is precisely in this low voltage region that VTe_2 shows a higher polarization as evidenced by the higher voltage increase and time span, *i.e.*, the height and width, of the relaxation steps. Results from GITT experiments were also employed to determine the diffusion coefficient of $AlCl_4^-$ ions (D_{AlCl4-}) using the following expression [81]:

$$D = \frac{4}{\pi t}\left(\frac{V_M\, m}{M\, S}\right)^2 \left(\frac{\Delta E_s}{\Delta E_t}\right)^2 \quad \text{Eq. 9}$$

where D is the diffusion coefficient, t is the time of the current pulse (300 s); V_M, m, M are the molar volume (43.9 $cm^3\ mol^{-1}$), the mass loading on the electrode (4.64 mg) and the molecular weight of the active material (306.4 g mol^{-1}) respectively; S is the area of the electrode in contact with the electrolyte (1.13 cm^2), ΔE_s is the voltage difference between the last point of two successive relaxations, and ΔE_t is the voltage difference resulting from the current pulse between them. For a better understanding, ΔE_s and ΔE_t from a single relaxation are illustrated in Fig. S12. Calculated D_{AlCl4-} values versus voltage are shown in Fig. S11b. At the charged state, 2.3 V, D_{AlCl4-} is 1.13×10^{-9} $cm^2\ s^{-1}$, which is the maximum value of the entire voltage range. Immediately, coinciding with the first plateau at 1.8 V, the diffusion coefficient decreases by four orders of magnitude, down to 7.64×10^{-13} $cm^2\ s^{-1}$, followed by an increase back to $10^{-10} - 10^{-11}$ $cm^2\ s^{-1}$ when the voltage plateau is completed. At the low voltage region, specifically during the second voltage plateau at 1.2 V, D_{AlCl4-} decreases again to even lower values reaching a minimum of 1.85×10^{-14} $cm^2\ s^{-1}$. From these results, it can be concluded that the diffusion of $AlCl_4^-$ is impeded when electrochemical processes are taking place, *i.e.*, in voltage plateaus. However, when the diffusion is not hindered, $VTe_2/Ti_3C_2T_x$ exhibits a D_{AlCl4-} of $10^{-9} - 10^{-10}$ $cm^2\ s^{-1}$, which is in agreement with other diffusion coefficient values reported for chalcogenides as cathodes for RABs [52,65,82]. Interestingly, considering the maximum and minimum values of D_{AlCl4-}, the diffusion process is most favored at high voltages, while it is most hindered at low voltages, with intermediate values in the middle voltage range, confirming the results obtained with the multi-scan rate experiment (Fig. 8).

4. Conclusions

In this work, VTe_2 has been proposed for the first time as a cathode for rechargeable aluminum batteries, as well as subjected to an improvement of its electrochemical performance by using $Ti_3C_2T_x$ MXene and mesoporous carbon CMK-3 modified separators. VTe_2 composite has been successfully synthesized via hydrothermal synthesis, as demonstrated by the XRD and elemental analysis. Regarding its electrochemical activity, VTe_2 undergoes 3 redox processes per (dis) charge in the 2.3 V–0.3 V voltage range vs. Al anode. *Ex situ* XPS and XRD experiments show that those electrochemical processes involve the redox pairs Te^{4+}/Te^{2-} and V^{5+}/V^{4+}. We propose that the charge transport within the VTe_2 cathode is based on $AlCl_4^-$ anions, which are inserted into the cathode during charge and leave the cathode during discharge. Cyclic voltammetry and diffusion coefficient determination by GITT indicate that the charge storage mechanism is dominated by surface-controlled processes at low voltages and by diffusion-controlled processes at high voltages. Electrochemical performance has been enhanced by the synergistic effect of $Ti_3C_2T_x$ and CMK-3, which can retain the soluble species generated upon charge on the cathode side and mitigate the shuttle effect of these species towards the anode. Cells with VTe_2 as the cathode and conventional separators exhibit total capacity degradation after 70 cycles at a current density of 100 mA g^{-1}. In contrast, cells utilizing a $VTe_2/Ti_3C_2T_x$ composite cathode combined with CMK-3 modified separators maintain a specific capacity of 63 mAh g^{-1} over 300 cycles under identical conditions. The results of this work pave the way for developing the potential of VTe_2 as a cathode material for rechargeable aluminum batteries, confirming the promising electrochemical properties of tellurides and chalcogenides. Future research should focus on how to remove impurities in the synthesized VTe_2 and optimize the CMK-3 coating of the separators to prevent the shuttle effect of soluble species. Concerning the prevention of the shuttle effect, approaches and strategies investigated in sulfur-batteries, such as the use of catalysts and wrapping the active materials with porous carbon structures, MXenes and others, can also be applied to TMCs as cathodes for RABs.

CRediT authorship contribution statement

Rafael Córdoba: Writing – original draft, Visualization, Methodology, Investigation, Formal analysis, Data curation, Conceptualization. **Ruocun (John) Wang:** Writing – review & editing, Validation, Methodology, Conceptualization. **Vanessa Trouillet:** Writing – review & editing, Formal analysis. **Sonia Dsoke:** Writing – review & editing, Visualization, Validation, Supervision, Methodology, Conceptualization.

Declaration of competing interest

The authors declare that they have no known competing financial interests or personal relationships that could have appeared to influence the work reported in this paper.

Acknowledgements

This work contributes to the research performed at CELEST (Center for Electrochemical Energy Storage Ulm-Karlsruhe) and was funded by the German Research Foundation (DFG) under Project ID 390874152 (POLiS Cluster of Excellence).

Appendix A. Supplementary data

Supplementary data to this article can be found online at https://doi.org/10.1016/j.jpowsour.2026.239403.

Data availability

Research data is available in KITopen/RADAR repository. It can be accessed here: https://publikationen.bibliothek.kit.edu/1000177694 and/or https://doi.org/10.35097/2ruyy6mx66tubd97

References

[1] H. Li, Z. Hu, Q. Xia, H. Zhang, Z. Li, H. Wang, X. Li, F. Zuo, F. Zhang, X. Wang, W. Ye, Q. Li, Y. Long, Q. Li, S. Yan, X. Liu, X. Zhang, G. Yu, G.-X. Miao, Adv. Mater. 33 (2021) 2170093.
[2] A. Huang, Y. Ma, J. Peng, L. Li, S. Chou, S. Ramakrishna, S. Peng, eScience 1 (2021) 141–162.
[3] S.-W. Kim, D.-H. Seo, X. Ma, G. Ceder, K. Kang, Adv. Energy Mater. 2 (2012) 710–721.
[4] C. Luo, Y. Xu, Y. Zhu, Y. Liu, S. Zheng, Y. Liu, A. Langrock, C. Wang, ACS Nano 7 (2013) 8003–8010.
[5] P.-F. Wang, Y. You, Y.-X. Yin, Y.-G. Guo, Adv. Energy Mater. 8 (2018) 1701912.
[6] K.W. Nam, S. Kim, S. Lee, M. Salama, I. Shterenberg, Y. Gofer, J.-S. Kim, E. Yang, C. S. Park, J.-S. Kim, S.-S. Lee, W.-S. Chang, S.-G. Doo, Y.N. Jo, Y. Jung, D. Aurbach, J. W. Choi, Nano Lett. 15 (2015) 4071–4079.
[7] Z. Jian, W. Luo, X. Ji, J. Am. Chem. Soc. 137 (2015) 11566–11569.
[8] J. Han, Y. Niu, S. Bao, Y.-N. Yu, S.-Y. Lu, M. Xu, Chem. Commun. 52 (2016) 11661–11664.
[9] A. Ponrouch, C. Frontera, F. Bardé, M.R. Palacín, Nat. Mater. 15 (2016) 169–172.
[10] X. Chen, C. Zhong, B. Liu, Z. Liu, X. Bi, N. Zhao, X. Han, Y. Deng, J. Lu, W. Hu, Small 14 (2018) 1702987.
[11] X. Chen, B. Liu, C. Zhong, Z. Liu, J. Liu, L. Ma, Y. Deng, X. Han, T. Wu, W. Hu, J. Lu, Adv. Energy Mater. 7 (2017) 1700779.
[12] M. Zhang, X. Song, X. Ou, Y. Tang, Energy Storage Mater. 16 (2019) 65–84.
[13] X. Zhang, Y. Tang, F. Zhang, C.-S. Lee, Adv. Energy Mater. 6 (2016) 1502588.
[14] H. Li, H. Yang, Z. Sun, Y. Shi, H.-M. Cheng, F. Li, Nano Energy 56 (2019) 100–108.
[15] H. Chen, F. Guo, Y. Liu, T. Huang, B. Zheng, N. Ananth, Z. Xu, W. Gao, C. Gao, Adv. Mater. 29 (2017) 1605958.
[16] G.A. Elia, K. Marquardt, K. Hoeppner, S. Fantini, R. Lin, E. Knipping, W. Peters, J.-F. Drillet, S. Passerini, R. Hahn, Adv. Mater. 28 (2016) 7564–7579.
[17] F. Ambroz, T.J. Macdonald, T. Nann, Adv. Energy Mater. 7 (2017) 1602093.
[18] E. Faegh, B. Ng, D. Hayman, W.E. Mustain, Nat. Energy 6 (2021) 21–29.
[19] M.-C. Lin, M. Gong, B. Lu, Y. Wu, D.-Y. Wang, M. Guan, M. Angell, C. Chen, J. Yang, B.-J. Hwang, H. Dai, Nature 520 (2015) 324–328.
[20] Y. Zhang, S. Liu, Y. Ji, J. Ma, H. Yu, Adv. Mater. 30 (2018) 1706310.
[21] N. Jayaprakash, S.K. Das, L.A. Archer, Chem. Commun. 47 (2011) 12610–12612.
[22] E. Fuentes-Mendoza, M. Talari, E. Zemlyanushin, R. Cordoba, N. Sabi, S. Dsoke, Chemelectrochem 12 (2025) e202400705.
[23] J. Wu, D. Wu, M. Zhao, Z. Wen, J. Jiang, J. Zeng, J. Zhao, Dalton Trans. 49 (2020) 729–736.
[24] L.-L. Chen, W.-L. Song, N. Li, H. Jiao, X. Han, Y. Luo, M. Wang, H. Chen, S. Jiao, D. Fang, Adv. Mater. 32 (2020) 2001212.
[25] E. Zemlyanushin, A.L. Müller, T. Tsuda, S. Dsoke, J. Electrochem. Soc. 171 (2024) 110507.
[26] A. Alazmi, P.M.F.J. Costa, J. Smajic, MRS Adv. 4 (2019) 807–812.
[27] L.D. Reed, E. Menke, J. Electrochem. Soc. 160 (2013) A915.
[28] H. Yang, H. Li, J. Li, Z. Sun, K. He, H.-M. Cheng, F. Li, Angew. Chem. Int. Ed. 58 (2019) 11978–11996.
[29] D.E. Couch, A. Brenner, J. Electrochem. Soc. 99 (1952) 234.
[30] F. Wu, H. Yang, Y. Bai, C. Wu, Adv. Mater. 31 (2019) 1806510.
[31] Y. Wu, M. Gong, M.-C. Lin, C. Yuan, M. Angell, L. Huang, D.-Y. Wang, X. Zhang, J. Yang, B.-J. Hwang, H. Dai, Adv. Mater. 28 (2016) 9218–9222.
[32] K. V Kravchyk, M. V Kovalenko, Commun. Chem. 3 (2020) 120.
[33] D.-Y. Wang, C.-Y. Wei, M.-C. Lin, C.-J. Pan, H.-L. Chou, H.-A. Chen, M. Gong, Y. Wu, C. Yuan, M. Angell, Y.-J. Hsieh, Y.-H. Chen, C.-Y. Wen, C.-W. Chen, B.-J. Hwang, C.-C. Chen, H. Dai, Nat. Commun. 8 (2017) 14283.
[34] J. Jiang, H. Li, J. Huang, K. Li, J. Zeng, Y. Yang, J. Li, Y. Wang, J. Wang, J. Zhao, ACS Appl. Mater. Interfaces 9 (2017) 28486–28494.
[35] H. Lu, Y. Wan, T. Wang, R. Jin, P. Ding, R. Wang, Y. Wang, C. Teng, L. Li, X. Wang, D. Zhou, G. Xue, J. Mater. Chem. A 7 (2019) 7213–7220.
[36] G. Studer, A. Schmidt, J. Büttner, M. Schmidt, A. Fischer, I. Krossing, B. Esser, Energy Environ. Sci. 16 (2023) 3760–3769.
[37] Z. Yu, S. Jiao, J. Tu, Y. Luo, W.-L. Song, H. Jiao, M. Wang, H. Chen, D. Fang, ACS Nano 14 (2020) 3469–3476.
[38] L. Wu, R. Sun, F. Xiong, C. Pei, K. Han, C. Peng, Y. Fan, W. Yang, Q. An, L. Mai, Phys. Chem. Chem. Phys. 20 (2018) 22563–22568.
[39] L. Xing, K.A. Owusu, X. Liu, J. Meng, K. Wang, Q. An, L. Mai, Nano Energy 79 (2021) 105384.
[40] X. Zhang, S. Wang, J. Tu, G. Zhang, S. Li, D. Tian, S. Jiao, ChemSusChem 11 (2018) 709–715.
[41] H. Lei, M. Wang, J. Tu, S. Jiao, Sustain. Energy Fuels 3 (2019) 2717–2724.
[42] C. Delmas, H. Cognac-Auradou, J.M. Cocciantelli, M. Ménétrier, J.P. Doumerc, Solid State Ion. 69 (1994) 257–264.
[43] R. Córdoba, A. Kuhn, J.C. Pérez-Flores, E. Morán, J.M. Gallardo-Amores, F. García-Alvarado, J. Power Sources 422 (2019) 42–48.
[44] X. Zhang, S. Jiao, J. Tu, W.-L. Song, X. Xiao, S. Li, M. Wang, H. Lei, D. Tian, H. Chen, D. Fang, Energy Environ. Sci. 12 (2019) 1918–1927.
[45] F. Tu, Y. Huo, J. Xie, G. Cao, T. Zhu, X. Zhao, S. Zhang, RSC Adv. 3 (2013) 23612–23619.
[46] M. Wang, Y. Song, Z. Sun, Y. Shao, C. Wei, Z. Xia, Z. Tian, Z. Liu, J. Sun, ACS Nano 13 (2019) 13235–13243.
[47] T.-C. Huang, K.-W. Cheng, C.-A. Lin, Y.-C. Fu, S.-K. Lin, Y.-Z. Chen, Sustain. Energy Fuels 6 (2022) 4626–4635.
[48] E. Ahmed, E. Ahrens, M. Heise, M. Ruck, Z. Anorg. Allg. Chem. 636 (2010) 2602–2606.
[49] J. Beck, Angew. Chem. Int. Ed. 33 (1994) 163–172.
[50] F.W. Poulsen, N.J. Bjerrum, O.F. Nielsen, Inorg. Chem. 13 (1974) 2693–2697.
[51] H. Gerding, H. Houtgraaf, Recl. Trav. Chim. Pay-B. 73, 1954, pp. 759–770.
[52] L. Chai, X. Li, W. Lv, G. Wu, W. Zhang, Z. Li, ACS Appl. Mater. Interfaces 14 (2022) 48780–48788.
[53] S.R. K. A., N. Barman, S. Radhakrishnan, R. Thapa, C.S. Rout, J. Mater. Chem. A 10 (2022) 23590–23602.
[54] T.S. Mathis, K. Maleski, A. Goad, A. Sarycheva, M. Anayee, A.C. Foucher, K. Hantanasirisakul, C.E. Shuck, E.A. Stach, Y. Gogotsi, ACS Nano 15 (2021) 6420–6429.
[55] S. Wang, K. V Kravchyk, A.N. Filippin, U. Müller, A.N. Tiwari, S. Buecheler, M. I. Bodnarchuk, M. V Kovalenko, Adv. Sci. 5 (2018) 1700712.
[56] Z. Zhou, N. Li, P. Wang, W.-L. Song, S. Jiao, H. Chen, D. Fang, J. Energy Chem. 42 (2020) 17–26.
[57] Z. Yu, Y. Xie, W. Wang, J. Hong, J. Ge, Front. Chem. 11 (2023) 1190102.
[58] The importance of basic electrochemistry terminology in the era of interdisciplinary battery research, Nat. Nanotechnol. 19 (2024) 1757. (Editorial).
[59] C. Xu, T. Diemant, A. Mariani, M.E. Di Pietro, A. Mele, X. Liu, S. Passerini, Angew. Chem. Int. Ed. 63 (2024) e202318204.
[60] K.D. Bronsema, G.W. Bus, G.A. Wiegers, J. Solid State Chem. 53 (1984) 415–421.
[61] J. Li, B. Zhao, P. Chen, R. Wu, B. Li, Q. Xia, G. Guo, J. Luo, K. Zang, Z. Zhang, H. Ma, G. Sun, X. Duan, X. Duan, Adv. Mater. 30 (2018) 1801043.
[62] H. Terrones, E. Del Corro, S. Feng, J.M. Poumirol, D. Rhodes, D. Smirnov, N. R. Pradhan, Z. Lin, M.A.T. Nguyen, A.L. Elías, T.E. Mallouk, L. Balicas, M. A. Pimenta, M. Terrones, Sci. Rep. 4 (2014) 4215.
[63] N. Sabi, K. Palanisamy, F. Rahide, S. Daboss, C. Kranz, S. Dsoke, Batter. Supercaps 6 (2023) e202300298.
[64] C. Zheng, J. Tu, S. Jiao, M. Wang, Z. Wang, ACS Appl. Energy Mater. 3 (2020) 12635–12643.
[65] C. Zhang, C. Lv, X. Yang, L. Chai, W. Zhang, Z. Li, ACS Appl. Mater. Interfaces 14 (2022) 37814–37822.
[66] N. Canever, F.R. Hughson, T. Nann, ACS Appl. Energy Mater. 3 (2020) 3673–3683.
[67] M. Shekhirev, C.E. Shuck, A. Sarycheva, Y. Gogotsi, Prog. Mater. Sci. 120 (2021) 100757.
[68] T. Hu, J. Wang, H. Zhang, Z. Li, M. Hu, X. Wang, Phys. Chem. Chem. Phys. 17 (2015) 9997–10003.
[69] H. Lei, J. Tu, W.-L. Song, H. Jiao, X. Xiao, S. Jiao, Inorg. Chem. Front. 8 (2021) 1030–1038.
[70] J. Wu, R. Wang, Q. Liu, M. Cheng, W. Ma, W. Liao, J. Hu, T. Wei, Y. Ling, B. Liu, M. Chen, W. Li, Compos. Commun. 45 (2024) 101795.
[71] J. Li, W. Liu, Z. Yu, J. Deng, S. Zhong, Q. Xiao, F. chen, D. Yan, Electrochim. Acta 370 (2021) 137790.
[72] K.L. Ng, B. Amrithraj, G. Azimi, Joule 6 (2022) 134–170.
[73] R. Córdoba, J. Goclon, A. Sarapulova, Q. Fu, J. Maibach, S. Dsoke, F. Fauth, A. Kuhn, F. García-Alvarado, Appl. Res. 2 (2022) e202200052.
[74] L. Zhang, Y. He, J. Bai, F. Liu, R. Bradley, W. Wu, X. Kong, S. Guo, Ceram. Int. 50 (2024) 32138–32146.
[75] L.-Å. Näslund, I. Persson, Appl. Surf. Sci. 593 (2022) 153442.
[76] A.J. Dent, A. Lees, R.J. Lewis, T. Welton, J. Chem Soc, Dalton Trans. 13 (1996) 2787–2792.
[77] B. Chen, H. Qin, K. Li, B. Zhang, E. Liu, N. Zhao, C. Shi, C. He, Nano Energy 66 (2019) 104133.
[78] Y. Shao, M.F. El-Kady, J. Sun, Y. Li, Q. Zhang, M. Zhu, H. Wang, B. Dunn, R. B. Kaner, Chem. Rev. 118 (2018) 9233–9280.
[79] H. Lindström, S. Södergren, A. Solbrand, H. Rensmo, J. Hjelm, A. Hagfeldt, S.-E. Lindquist, J. Phys. Chem. B 101 (1997) 7717–7722.
[80] C.N. Gannett, L. Melecio-Zambrano, M.J. Theibault, B.M. Peterson, B.P. Fors, H. D. Abruña, Mater. Rep.: Energy. 1 (2021) 100008.
[81] W. Weppner, R.A. Huggins, J. Electrochem. Soc. 124 (1977) 1569.
[82] Y. Du, B. Zhang, W. Zhang, H. Jin, J. Qin, J. Wan, J. Zhang, G. Chen, Energy Storage Mater. 38 (2021) 231–240.